ELSEVIER

Nuclear Instruments and Methods in Physics Research A 401 (1997) 63–80

NUCLEAR INSTRUMENTS & METHODS IN PHYSICS RESEARCH Section A

The small angle rear tracking detector of ZEUS

A. Bamberger[a,1], H. Boterenbrood[b,2], J. Bulmahn[c,3], R. Carlin[d,4], H. Cunitz[e,3], J. Dawson[f,5], M. de Kamps[b,2], W. Hain[g], D. Hanna[h,6], J. Hauschildt[g], R. Klanner[i,1], U. Kötz[g], A. Kruse[b,2], J.N. Lim[h,6], M. Morandin[d,4], J.S.T. Ng[g,*], J.R. Okrasinski[f,5], J. Parsons[e,3], G. Pitacco[d,4], J. Repond[f,5], S. Ritz[e,3], M. Rohde[g], J. Schlereth[f,5], W. Schott[i,1], R. Talaga[f,5], H. Tiecke[b,2], W. Verkerke[b,2], J.J. Whitmore[c,3]

[a] *Fakultät für Physik der Universität Freiburg i.Br., Freiburg i.Br., Germany*
[b] *NIKHEF and University of Amsterdam, Netherlands*
[c] *Pennsylvania State University, University Park, PA, USA*
[d] *Dipartimento di Fisica dell' Universita and INFN, Padova, Italy*
[e] *Columbia University, Nevis Labs., Irvington on Hudson, NY, USA*
[f] *Argonne National Laboratory, Argonne, IL, USA*
[g] *Deutsches Elektronen-Synchrotron DESY, 22604 Hamburg, Germany*
[h] *McGill University, Dept. of Physics, Montreal, Quebec, Canada*
[i] *Hamburg University, II. Institute of Exp. Physics, Hamburg, Germany*

Received 14 August 1997

Abstract

The design, construction, installation, and performance of the small angle rear tracking detector of the ZEUS experiment are described. The results on electron position measurement, electron energy correction, and background reduction at the first-level trigger are presented. The impact on the measurement of the proton structure function is discussed.

PACS: 29.40.Gx; 29.40.Mc; 29.40.Vj; 13.60.Hb
Keywords: Scintillator hodoscope; Pre-showering correction; Timing veto

1. Introduction

The ZEUS experiment at the HERA electron–proton collider at DESY has been taking data since 1992 [1]. The small angle rear tracking detector (SRTD), consisting of finely segmented scintillator strips, was installed in ZEUS in 1994. The SRTD was constructed with the purpose of improving the electron and other charged-particle measurement in the small-angle region around the beam pipe in the rear

* Corresponding author. Tel.: +49 40 8998 3030; fax: +49 40 8998 3094; e-mail: ng@desy.de.

[1] Supported by the German Federal Ministry for Education and Research (BMBF).
[2] Supported by the Netherlands Foundation for Research on Matter (FOM).
[3] Supported by the US National Science Foundation.
[4] Supported by the Italian National Institute for Nuclear Physics (INFN).
[5] Supported by the US Department of Energy.
[6] Supported by the NSERC and FCAR of Canada.

PII S0168-9002(97)01029-2

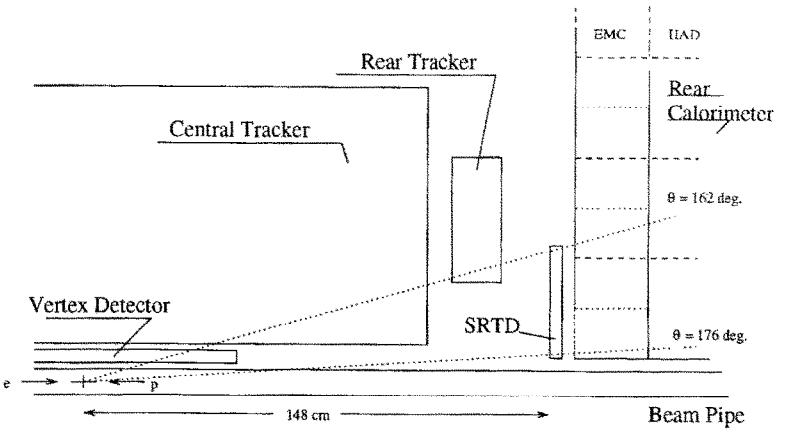

Fig. 1. A side view of part of the ZEUS detector in the rear direction (not to scale).

(electron beam) direction. In addition, the SRTD also provides fast timing at the first-level trigger to reject backgrounds from proton interactions upstream.

The deep inelastic scattering (DIS) process $e+p \rightarrow e'+X$ is generally studied in terms of Q^2, the negative of the four-momentum transfer squared, and Bjorken x, the momentum fraction of the struck quark. One of the most important results to emerge from the HERA physics program so far is the observation of the rapid rise of the proton structure function $F_2(x, Q^2)$ with decreasing x for $x \leq 10^{-2}$ at fixed Q^2, and it is of great interest to extend the measurements to the region $x < 10^{-4}$ to study the low x behavior [2]. In the ZEUS experiment, because of the almost hermetic coverage, both the scattered electron and hadronic system are measured, which provide two independent determinations of x and Q^2. And in the kinematic region of interest, these variables are more reliably reconstructed using the measured energy (E'_e) and angle (θ) of the scattered electron:

$$Q^2 = 4E_e E'_e \cos^2(\theta/2), \tag{1}$$

$$x = \frac{E_e E'_e \cos^2(\theta/2)}{E_p(E_e - E'_e \sin^2(\theta/2))}, \tag{2}$$

where E_e and E_p are the electron and proton beam energies, and θ is measured with respect to the proton beam (Z-axis) direction.

Much of this region, corresponding to $\theta > 165°$, was not covered by the existing tracking detectors of the ZEUS experiment, so the precision of the electron position determination was limited (see Fig. 1). The precise determination of the electron impact position is required for the reconstruction of kinematic variables, and for fiducial definition for shower containment close to the calorimeter boundary around the beam pipe. Furthermore, there was a significant amount of inactive material close to the beam pipe which caused essentially all the electrons to shower before reaching the calorimeter, resulting in an inaccurate determination of the electron energy.

Backgrounds also have a significant impact on DIS measurements. The large rate from upstream proton beam–gas interactions has been reduced at the ZEUS first-level trigger (FLT) by existing veto counters which, however, have a limited acceptance. The timing of the energy deposits in the rear calorimeter (RCAL) from upstream interactions is early by approximately 10 ns compared to the nominal timing of energy deposits from electron–proton (ep) collisions. The RCAL timing is not available at the FLT, where the trigger decision must be made 4.4 μs after the colliding beams cross, but is used to reject backgrounds at later trigger levels. To reduce the FLT background rate, it was necessary to raise the trigger energy thresholds in the RCAL beam pipe region, leading to a reduced acceptance for low x events.

The SRTD was designed to:

- improve the position measurement and identification of charged particles within the acceptance of the SRTD;

- identify pre-showering electrons with the possibility to correct for energy loss in the inactive material; and
- identify upstream proton beam–gas interactions based on timing at the FLT level.

In order to achieve these objectives, the SRTD is required to have:

- position resolution <5 mm;
- timing resolution <1 ns;
- efficiency for minimum ionizing particles (MIP) $>99\%$;
- energy resolution <1 MIP;
- energy scale calibration uncertainty $<10\%$;
- event timing at the first-level trigger; and
- energy and time information for offline analysis.

Given the severe constraints presented by the already existing ZEUS detector:

- <5 cm of space between the RCAL and the mechanical support structure of the central components,
- regular movement of the RCAL to avoid radiation damage of the calorimeter during beam injection and acceleration, and
- magnetic fields of 1.4 T,

two layers of plastic scintillator strips read out by optical fibers and photomultipliers were chosen to implement the SRTD.

In this paper, the design, construction, installation, and performance of the SRTD are described. The mechanical layout is presented in Section 2. The optical readout is discussed in Section 3. A description of the front-end electronics and calibration is given in Section 4. Finally, the offline data analysis and results on the performance of the SRTD are presented in Sections 5 and 6, respectively.

2. Mechanical layout

2.1. Overview

In the active part of the SRTD, the scintillator strips are arranged in two overlapping layers, one containing horizontal, the other vertical strips. In the X–Y plane, the SRTD is divided into four quadrants, 24 cm × 44 cm each as shown in Fig. 2. The detector covers a total area of 68 cm × 68 cm, except for the 20 cm × 20 cm cutout in the center for the beam pipe.[7] The angular coverage is $162° < \theta < 176°$, with complete acceptance for $167° < \theta < 174.5°$. There is a total of 272 channels.

Scintillator was chosen as the detector material for its fast timing response and its high efficiency for minimum ionizing particles. The scintillation light is detected by photomultipliers (PMTs) via light guides. The light guides were made from bundles of optical fibers for optimal transmission efficiency. Space for housing the PMTs and front-end electronics was available on the sides of the RCAL at approximately 2.5 m distance from the active detector. Constrained by the available space (in the Z-dimension) in the SRTD active region, the thickness of the scintillator strips was chosen to be 5 mm, resulting in a thickness of 15 mm for the entire system including the mechanical support. A side view of part of the ZEUS detector is shown in Fig. 1, indicating the position of the SRTD at $Z = -148$ cm from the nominal interaction point. A perspective view of the SRTD after installation is shown in Fig. 3.

2.2. Scintillator strips

The scintillator material SCSN-38 was chosen. The same material was used in the ZEUS uranium-scintillator calorimeter [1]. The strips were diamond cut and polished with high precision on the dimensions and angles and with high-quality surfaces.[8] The strip cross section was 5.0 ± 0.2 mm by 9.80 ± 0.05 mm. As shown in Fig. 2, two lengths, 240.0 ± 0.2 mm and 440.0 ± 0.2 mm were used. One end of each strip was aluminized by vacuum deposition[9] providing a reflective mirror to improve the light output and the response uniformity.

2.3. Light guides

The light guides were made from clear PMMA fibers (Hoechst Infolite FK52). These are single-clad, 1 mm diameter fibers with a minimum bending radius of 25 mm. For easy handling of the light guides, the

[7] In 1995 the vertical gap of the RCAL in the beam pipe region was reduced from 20 to 8 cm and the SRTD geometry was adjusted accordingly without changing the quadrant size.

[8] Gebex AG, Uster, Switzerland.

[9] Precitrame SA, Tramelan, Switzerland.

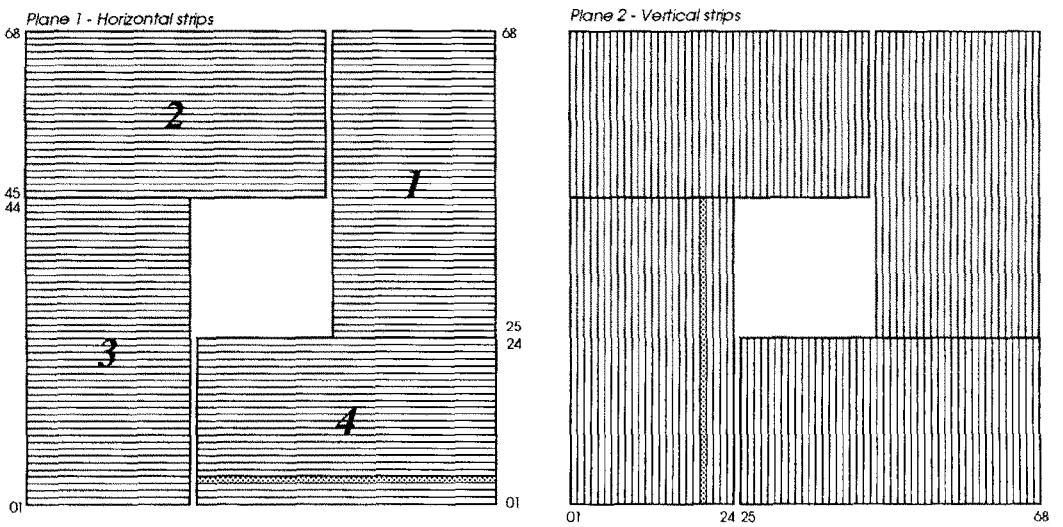

Fig. 2. Arrangement of the two layers of scintillator strips. One strip from each layer is shaded for illustration.

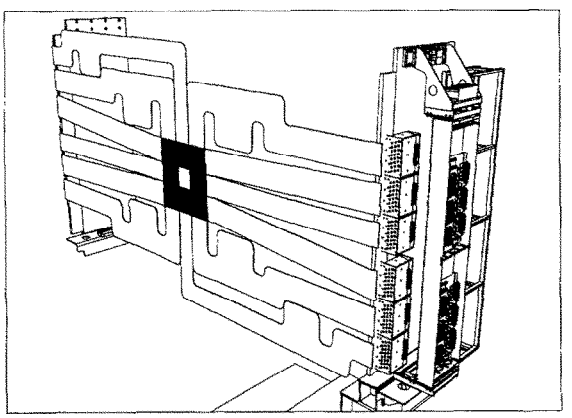

Fig. 3. A perspective view of the SRTD installed in ZEUS. The scintillator strips are located in the dark-square area near the center. Scintillation light is transported via light guides to PMTs housed at the sides of the RCAL, where the support for the front-end electronics is also located.

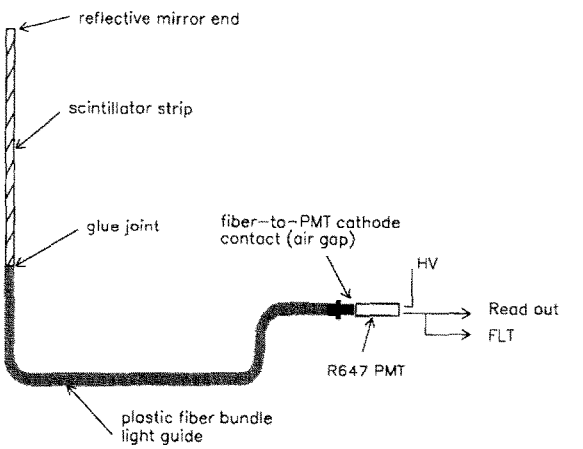

Fig. 4. A schematic layout for one SRTD detector channel (not to scale).

fibers were glued together to form a solid piece. For the construction, a bundle of 45 fibers was cut to the appropriate length (2.1–3.5 m), and then glued to form the required shape. During this procedure, care was taken so that the fibers of an individual bundle remain in a close-packed configuration with a minimal cross section of 8.0 mm×5.4 mm. Any irregularity in the fiber bundle would result in an increase in the space taken by the detector. The fibers were held in place by a series of straight and circular Teflon jigs, and soaked with the glue HT-2 (R&G), with 24 h curing time. At one end of the light guide, the fiber bundle was glued together to form a rectangular cross section of 9.5 mm × 4.6 mm matching that of the scintillator strip; while at the other end, with one additional fiber for laser light, the bundle was glued into a cylindrical shell of black lucite to form a connector to the PMT housing. The glue used in this step was Stycast 1264 (Emerson & Cuming), with 48 h curing time. Both ends of the fiber bundle were cut and polished with a diamond mill.

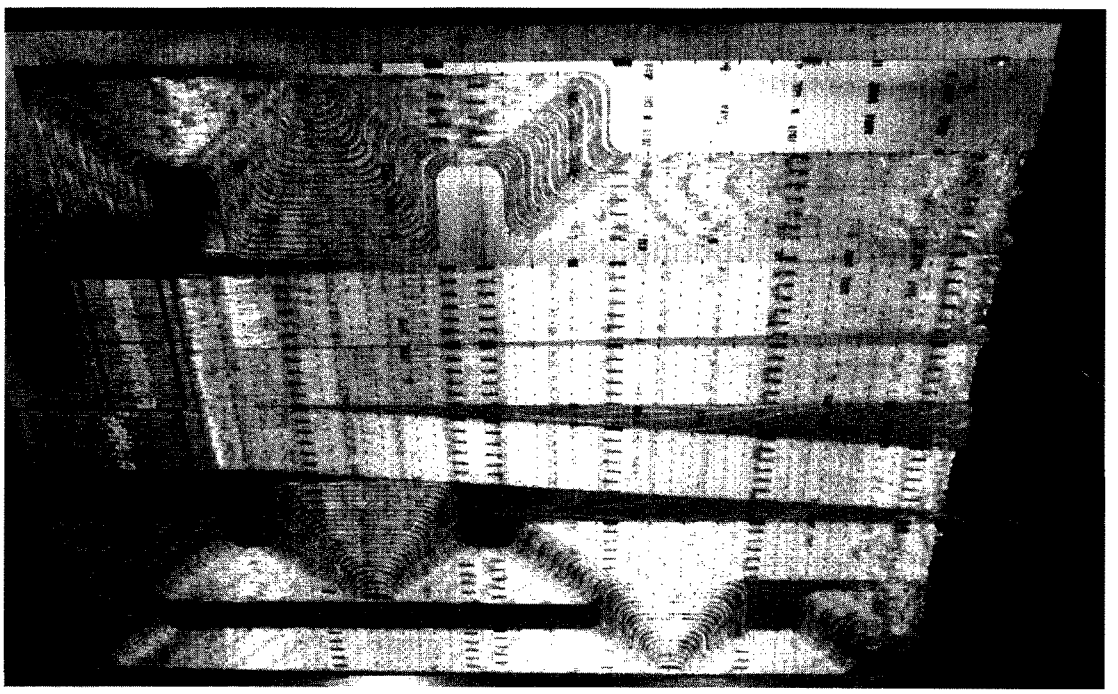

Fig. 5. A photograph of one-half of the SRTD with the top cover removed. The layer of horizontal strips is visible near the center left. The vertical strips are situated beneath the horizontal ones. Also shown are the light guides grouped into equal lengths leading from the strips to the PMTs (not shown) located along the right edge of the support structure.

A detector channel was completed by gluing the light guide to the scintillator strip using Loctite 401, with 5 min curing time. The scintillator and part of the light guide (a few millimeters in length) were wrapped with one layer of 27 μm thick aluminium foil to avoid light coupling to the neighboring channels. No adverse chemical effects of the glue on the scintillator or the fiber were observed. As discussed in Section 3.3, the response to a single MIP was measured for each completed channel to ensure the quality of the detector, to determine the response uniformity along the strip, and to obtain a measurement of the conversion factors between signal charge (pC) to particle count (MIPs). Fig. 4 shows a schematic view of one complete detector channel.

The light guides of a given group of strips were made of equal lengths to ensure equal arrival time of the scintillation light at the PMTs approximately 2.5 m away, in order to improve the relative timing at the FLT. As a result, the light guides for the vertical strips were routed in a curved fashion (trombone design) to account for the varying distances to the PMTs. This can be seen in a photograph of one-half of the completed SRTD in Fig. 5. The layer of horizontal scintillator strips can be seen connected to three groups of straight light guides. The layer of vertical strips, hidden from view by the horizontal strips, are connected to three groups of curved (trombone) light guides.

2.4. *Support structure*

The SRTD support structure is divided into two independent halves, one for each half of the RCAL. Each structure consists of two large 1 mm thick aluminium sheets, with one additional sheet in the active region separating the two layers of scintillator strips. The amount of material in the active region corresponds to 0.06 radiation lengths. The aluminium sheets are separated by brass spacers and held together by screws. The spacers also keep the light guides in place. Each plane of 24 or 44 scintillator strips of a quadrant is fixed with two tension straps (0.2 mm thick steel) which are in turn attached to the support structure.

The resulting relative positioning of the strips is then well defined and is maintained to a 0.2 mm accuracy. The separation between the aluminium sheets is 6 mm, sufficient to contain the wrapped scintillator strips, as well as the tension straps. Each structure is mounted onto the front face of the RCAL with steel rods which are attached to the top and the bottom of the calorimeter support structure, and held in place with an additional tension strap attached to the sides of the calorimeter. One-half of the completed SRTD is shown in Fig. 5, with the top sheet of the support structure removed. The SRTD as installed in ZEUS is shown in a perspective view in Fig. 3.

3. Optical readout

3.1. Photomultipliers and high-voltage system

The dimensions of the PMTs for the SRTD read-out are restricted because of the limited space available for magnetic shielding and mechanical support. The Hamamatsu R647 PMT was chosen mainly for this reason. It is a $\frac{1}{2}$ in. diameter, bialkali-cathode, 10-dynode-stage tube with a 2.5 ns rise time, suitable for the fast timing measurements for the first-level trigger. The PMTs are mounted in iron boxes (up to 24 per box) with 10 mm thick walls to provide magnetic shielding. Tests in the ZEUS environment did not show any gain change after the magnets were switched on. No optimization of the wall thickness was done. A photograph of the box with 24 PMTs installed is shown in Fig. 6. Each PMT has its own μ-metal shielding. A spring presses the PMT against the fiber light guide.

A Cockroft–Walton voltage multiplier generates the high voltage directly at the PMT bases [3–5]. Three input voltages, ± 18 and 5 V are required. This system has a lower power dissipation and lower output impedance than a source with a passive divider chain. There are three HV generators in each box with one microprocessor for remote control. A flat cable provides the HV for the individual dynodes. The high-voltage generator and controller are mounted on the lid of the PMT box, which opens freely for servicing, as can be seen from Fig. 6. Eight PMTs are daisy-chained together, and consequently, operate at the same HV. In fact, the same high voltage is used for the group of 20 or 24 PMTs in each box in order to obtain similar transit times, and thus, improved relative timing.

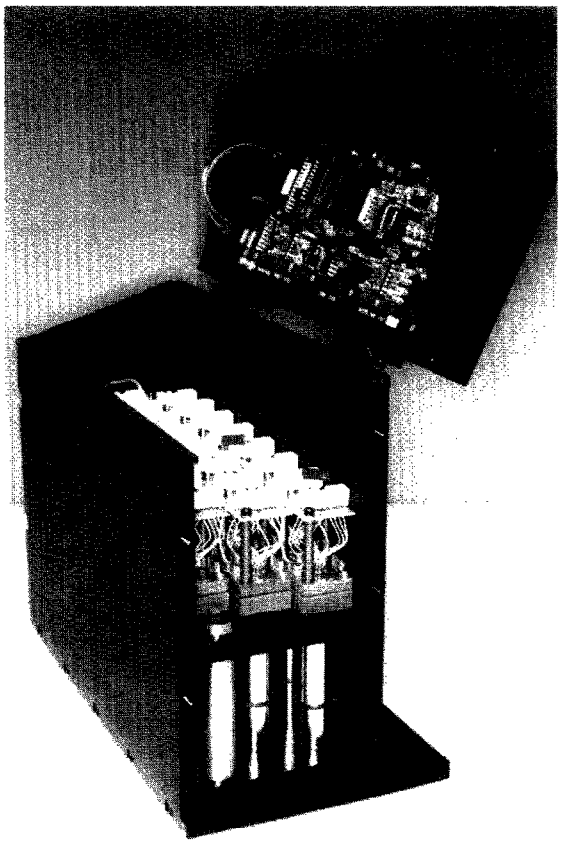

Fig. 6. A photograph of the PMT box. A side plate has been removed and the lid opened to show clearly the interior layout. The PMTs are shown facing downwards in the picture.

The PMT gain setting and HV base configuration were chosen according to the pulse-height threshold in the SRTD FLT and the read-out dynamic range. For a 50 Ω input impedance and a signal FWHM of 10 ns, the chosen scale of 2.5 pC/MIP provides a MIP signal pulse height of approximately 12.5 mV at the FLT. For a nominal light yield of 25 photoelectrons per MIP, a gain of 6.25×10^5 is required. Monte Carlo studies showed that for pre-showering electrons, on average 50 MIPs are detected in a single SRTD strip, with a maximum of more than 100 MIPs. The voltage distribution ratio 2 : 1 : 1 : 1 : 1 : 1 : 1 : 2 : 2 : 2 : 3 was chosen to improve the linearity of the R647 for large anode pulses. This divider configuration gives a satisfactory nonlinearity below 10% for an anode signal of 100 pC.

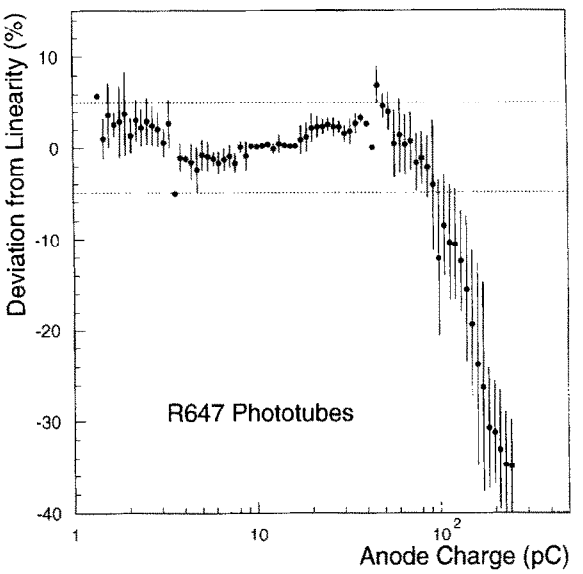

Fig. 7. The average nonlinearity of a sample of R647 PMTs as a function of anode charge. The error bars indicate the spread in nonlinearity among the PMTs.

However, it also gives a lower gain than the linear base at the same HV. The gain specification to the vendors was $G \geq 3 \times 10^6$ at 1000 V (measured with a linear voltage distribution), allowing the required gain to be obtained with the chosen voltage distribution at voltages below the maximum rating.

3.2. Photomultiplier tests

The PMT gain, linearity and dark current were measured before installation using a system built for testing the ZEUS calorimeter PMTs [6]. In this system, light from a DC light source, a pulsed green LED, or a blue Nitrogen-dye laser was used. The light intensity was varied using two filter wheels with eight different attenuation levels, and monitored by two Si-diodes. The light level, readout electronics, and the high voltage were under computer control.

The PMT gain was determined from the response to well-defined light levels at six high-voltage settings, ranging from 650 to 1000 V. The ADC pulse height can be related to the gain through the number of photoelectrons given by the width of the pulse-height spectrum. A fit of the gain as a function of high voltage (H), $G = a \times H^b$, was performed and the fitted parameters were used for gain calculations.

The linearity was determined by measuring the PMT responses to varying input-light levels at nominal gain. The laser intensity was adjusted by neutral-density filters. The measured average PMT response nonlinearity as a function of anode charge is shown in Fig. 7. The error bars indicate the spread in the measurements for this sample of PMTs. The two dotted lines bracket the ±5% nonlinearity range.

The dark current was measured by integrating the PMT pulses over a wide gate (500 ns) under no-light condition at several high voltages around the nominal setting. The data points were fitted to $I_{\text{dark}} = c \times H^d$ and extrapolated to the HV setting for nominal gain. The maximum and the average dark current measured was 5 and 1 nA, respectively.

3.3. Light-yield measurement

The MIP response of each SRTD channel was measured using a collimated ^{106}Ru source placed on top of the strip, with a trigger counter placed below. One standard PMT, an XP1911 (Valvo), was used for all channels. The photoelectron calibration was obtained using an LED. The width of the LED spectrum was assumed to be due to photostatistics. This resulted in a lower limit on the actual number of photoelectrons since additional fluctuations of the pulse amplitudes not related to photostatistics were included. The average measured response was 27 photoelectrons for the horizontal strips readout via straight light guides, and 10 photoelectrons for the vertical strips read out via curved (trombone) light guides.

The nominal MIP calibration was obtained with the source located at 15 cm distance from the light-guide contact. For a subset of the channels, the light yield was also measured with the source placed at several points along the strip. The response along the strip is uniform to better than 10% up to 2 cm from the light guide, where it increases up to 20%.

The PMT gain and detector light yield were matched to give a uniform MIP signal for all channels. For each detector channel in a high-voltage group, a matching PMT was found such that the MIP response was closest to 2.5 pC. This was repeated for a range of HV settings. For a given group of channels, the matching arrangement with the minimal spread in MIP response was chosen. An average of 2.5 pC and an rms spread of less than 3% were

measured for the MIP responses of all channels. The HV settings were chosen with values ranging from 800 to 950 V, well below the maximum rating of 1250 V.

4. Front-end electronics

4.1. Readout electronics

The SRTD read-out electronics is similar to that used for the ZEUS calorimeter. A detailed description can be found elsewhere [7]. The analog part of the readout is located on the detector. On the read-out front-end cards, the fast PMT signal is split into a high- and a low-gain channel, pulse shaped, sampled and stored in an analog pipeline. If the event is to be read out, the sampled voltage levels are stored in an analog buffer, and then multiplexed via long cables to the ADCs on the digital cards located in counting rooms away from the detector. The calculations of the energy, time, and other quantities from the digitized samples are done in a digital signal processor on the digital card. The readout ADC saturation limit is 2200 pC which corresponds to approximately 1000 MIPs.

4.2. First-level trigger

At HERA, the colliding beams cross every 96 ns. The ZEUS global first-level trigger (GFLT) decision is made 46 crossings or 4.4 μs after the collision. The SRTD first-level trigger provides fast timing information for rejection of upstream proton beam–gas interactions. As shown in Fig. 4, the PMT signal is sent to both the readout and the FLT. The high impedance of the input amplifiers on the trigger cards allows spying on the signal as it propagates from the PMT to the readout electronics where the signal is terminated in 50 Ω. A dual-threshold discriminator is used to achieve good timing resolution. The low-threshold signal is delayed and used in coincidence with the high-threshold signal. The low-threshold crossing time gives the timing. This scheme reduces the time walk due to pulse-height variations. In tests with a prototype detector, with threshold settings at 0.1 and 0.3 MIP, a timing resolution of 1 ns was measured.

4.2.1. SRTD FLT in 1994

A subset of the SRTD channels was instrumented for the FLT during the 1994 running period. For each SRTD quadrant, the group of eight 44 cm long strips closest to the beam pipe was connected to a trigger card. There were 4 trigger cards, 8 channels each, made with two-layer printed-circuit boards.

Each board has an analog section with dual-threshold discriminators, and a digital section which controls the threshold and channel mask on/off settings. An individual channel can be masked off in case of noise or other problems, but the threshold is the same for all 8 channels on each board. The threshold and channel mask settings are downloaded as serial data remotely via an 8-pair Scotchflex cable. The settings are kept by on-board registers. Manual setting of the threshold and channel mask is also possible for test purposes. The LeCroy MVL407 four fold op-amp chip is used as the high impedance dual-threshold discriminator. The low-threshold discriminator output signal is delayed via a coaxial cable. The logical OR of the 8 high/low coincidence outputs, where the earliest time in the 8 channels determines the timing, is sent out as a NIM signal via a cable driver. The relative timing offsets of the 8 channels on each board were obtained using beam–gas data collected when only the electron or proton beam circulated. Each channel was masked off one at a time, and its timing determined and corrected with delay cables. The relative timing was tuned to better than 1 ns. These NIM signals from the 4 trigger cards were sent to the ZEUS GFLT for timing veto decisions and monitoring for each beam crossing.

4.2.2. SRTD FLT since 1995

The SRTD has been fully instrumented for the FLT since the beginning of the 1995 running period [8]. For each SRTD quadrant, the group of 24 long (44 cm) strips is connected to one trigger card, and the group of 44 short (24 cm) strips is connected to two others. There are 12 trigger cards located in the detector adjacent to the RCAL. Each set of 3 trigger cards per SRTD quadrant is controlled by a 9U VME card located in the counting room via a 40 m long ribbon twisted pair data bus. Resident in the same VME crate is an MVME147 processor with an Ethernet connection running under OS9 and a ZEUS transputer

module connected to the central data acquisition system for read out from the SRTD FLT in the event of a second-level accept.

The trigger cards are implemented in ECL and CMOS with 24 channels per card on 12-layer printed circuit boards. Each card has an analog section with dual-threshold discriminators, and a digital section which controls the threshold and channel mask on/off settings. The National 100314 chips are used as the high-impedance amplifier/discriminators. An individual channel can be masked off in case of noise or other problems. Both the high and the low thresholds can be set for each channel. But, in practice, most of the channels have the same threshold setting, and only some thresholds are different, as required to keep the singles rate down. The threshold- and channel-mask settings are downloaded through the data bus from the VME crate. All parameters of the trigger cards are retained in on-board registers and an extensive repertoire of diagnostic software has been developed.

The timing data are generated by an on-board rapid cycling TDC. The TDC output has a dynamic range of 63 ns, encoded in 6 bits with the least significant bit approximately equal to 1 ns. The relative timing of each channel is adjusted with plug-in passive delays. The TDC is started every 96 ns by a signal synchronous with the HERA clock and stopped by either a coincidence signal between the overlapping scintillator layers or, if there is no coincidence signal within 63 ns of start, by a default overflow signal. The low-threshold discriminator output determines the timing and the high-threshold output is used to define a hit. The coincidence signal is generated when there is a hit in both layers in a given quadrant within 15 ns of each other. The TDC output is sent to the GFLT on each beam crossing.

4.3. Online calibrations and monitoring

Test signals are used for the diagnostics and calibrations of the front-end electronics. These signals are generated either via precision charge injection into the readout front-end cards and the trigger cards, or via laser pulses brought to the PMT entrance window via a light fiber. The gain, pedestal and linearity of the readout electronics are measured regularly and correction factors are downloaded to the readout system. For the SRTD FLT, the test signals provide calibration data for the coincidence timing and diagnostics for the trigger channels.

The high-voltage settings are continuously monitored and maintained at a constant level by a microprocessor in the HV generator system. The gain variations over the entire running period are negligible, as indicated by offline data (see Section 5.1).

5. Offline data analysis

5.1. The SRTD energy scale

The energy deposit in the SRTD is measured in units of MIPs. An initial charge-to-MIP calibration is obtained using a ^{106}Ru source. The final energy scale calibration for every channel is obtained from ep data, using events with an isolated MIP-like particle found in the SRTD. These events are selected by requiring that only one strip is hit in each of the two overlapping layers, and that the energy deposit in one of the strips is above threshold to suppress noise. The energy deposit in the other strip is used to determine its MIP response. The MIP energy distribution is fitted to the function [9]:

$$f(\lambda) = A\mathrm{e}^{-1/2(\lambda+\mathrm{e}^{-\lambda})}, \tag{3}$$

where $\lambda = (E - E_{\mathrm{MIP}})/B$, and A, B, and E_{MIP} are the free parameters. For each channel, the MIP scale is given by the fitted value of E_{MIP}, which is approximately the most probable value of energy loss by a MIP in the scintillator strip. Some typical distributions are shown in Fig. 8. With this method, the average MIP scale is measured to be approximately 2.8 pC/MIP with a 16% rms spread. These values are slightly different from those obtained in the initial light-yield measurement (see Section 3.3). This can be explained by the fact that the initial measurement did not include effects due to the quantum efficiencies of the PMTs installed in the experiment. The MIP scale values are also determined for three separate time periods during the 1994 run, and are stable to better than 5%. Based on these studies, an accuracy of approximately 10% is estimated for the SRTD energy scale, which is adequate for the purpose of electron energy loss correction. The electronics noise, measured from the energy distribution of strips with no energy deposit, is approximately 1.4% of a MIP.

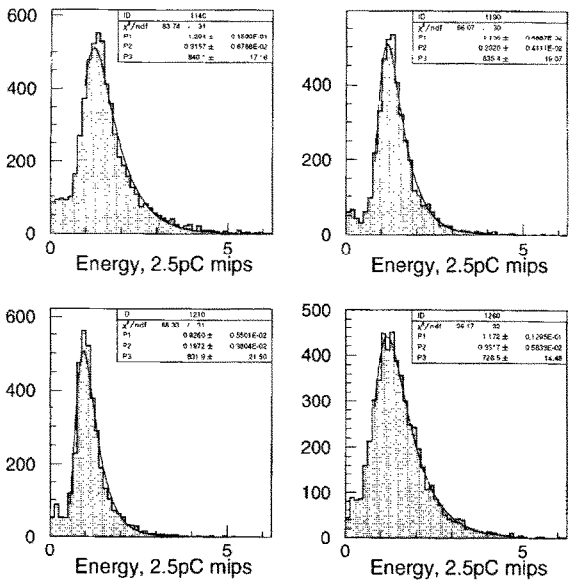

Fig. 8. The SRTD MIP energy distributions in four typical channels. An initial calibration of 2.5 pC/MIP is used. The variation in widths is due to the difference in light yield. The fitted curves are also shown.

5.2. Offline timing measurement

The offline event timing in each channel is corrected for several effects. The relative time delays from the light guide and cable lengths are calculated assuming a signal propagation speed of 0.6 c in both cases. Residual time offsets as well as the pulse-height dependence of time measurements are determined using ep data for each channel.

The timing measurement is studied using a sample of DIS events with an electron found in the SRTD. For all channels, the dependence of the reconstructed time on the energy deposit in the SRTD is found to be smaller than 0.5 ns, and therefore, no corrections are used. The single-strip timing resolution is shown in Fig. 9 as a function of strip energy for several channels. It is parametrized by $\sigma_0/\sqrt{E}$, where E is the strip energy, and σ_0 the fitted Gaussian width of the timing distribution at a given E. The average values for σ_0 are 3.6 and 5.2 ($\mathrm{ns}\sqrt{\mathrm{MIP}}$) for E between 0.2 and 20 MIPs, for the two groups of strips coupled to straight and curved light guides, respectively. The corresponding rms spreads in σ_0 are 0.3 and 0.9 ($\mathrm{ns}\sqrt{\mathrm{MIP}}$).

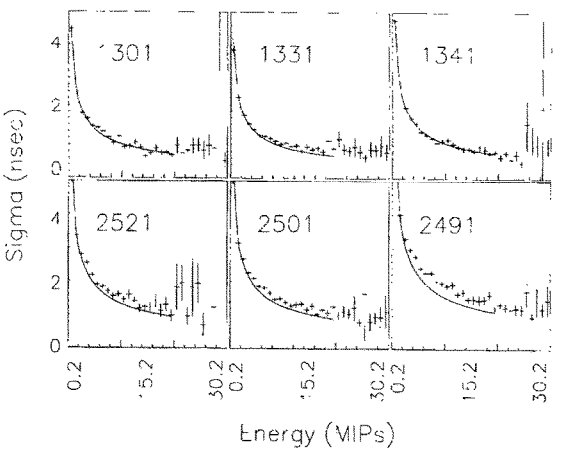

Fig. 9. Single-strip timing resolution for a sample of strips measured using DIS data with an electron hit in the SRTD.

To account for any residual time offsets from the combined effect of PMT transit time and delays in the readout electronics, an average strip time is calculated for events from a dedicated data sample. Effects due to HERA beam timing shifts are taken into account. The average strip time for all events with strip energy between 2 and 18 MIPs is measured by: $\bar{t}_{\mathrm{strip}} = \sum t_{\mathrm{strip}}(E/\sigma_0^2)/\sum(E/\sigma_0^2)$. The time offsets are typically inside a ± 2 ns range.

6. Results on the SRTD performance

The capabilities of the SRTD are illustrated with two typical DIS events. In the event shown in Fig. 10, there is a clean isolated electron hit in the SRTD. The matching between the SRTD hits and the energy deposits in the calorimeter is clear. The fine segmentation provides improved electron position determination. In the event shown in Fig. 11, the scattered electron as well as a jet of hadronic particles are observed in the SRTD region. The electron is also clearly matched to the SRTD hits. For these nonisolated events, adequate segmentation is required in order to correctly assign the SRTD hits to the scattered electron. This is important both for position reconstruction and for electron energy loss correction.

6.1. Electron position measurement

Because of the fine segmentation, the SRTD electron position measurement has a better resolution and

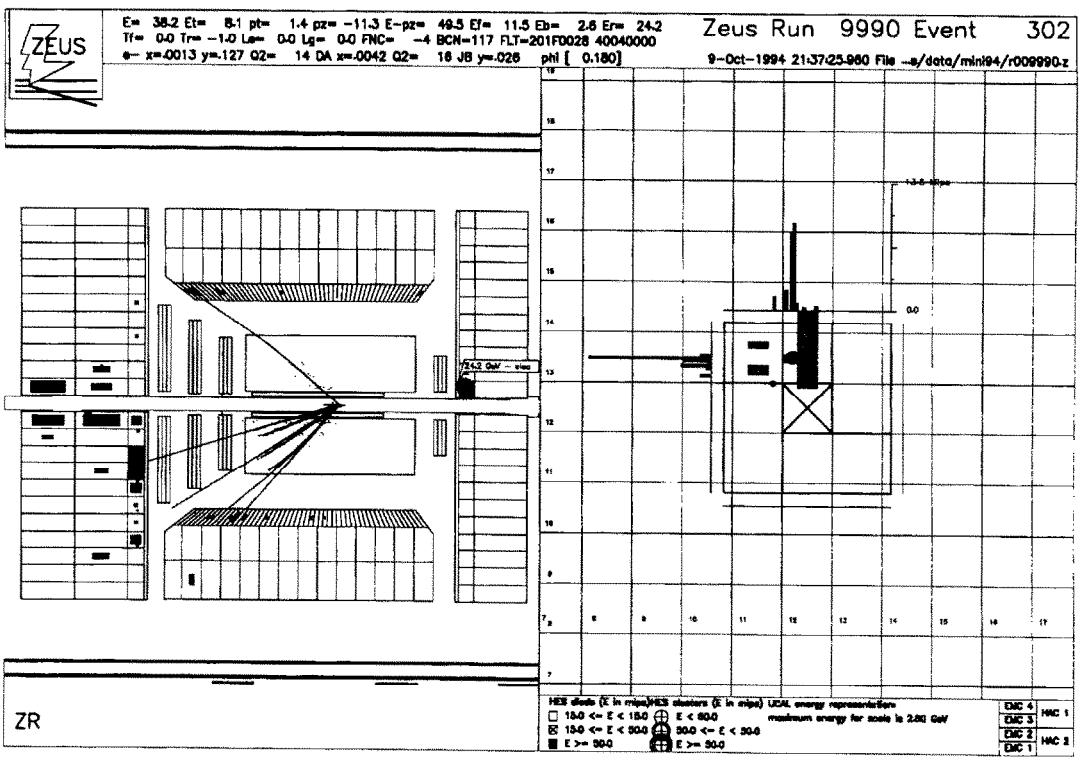

Fig. 10. A typical DIS event with an isolated electron in the SRTD. In the side view (left), the proton beam points to the left, and the scattered electron is detected just above the beam pipe in front of the RCAL. In the X–Y view (right), the energy deposits in the SRTD strips are shown by the histograms where each bin corresponds to a strip; the energy deposits in the RCAL are shown as dark rectangles.

a smaller systematic shift, on average, than the calorimeter. The position resolution is determined from the data, using DIS electrons with impact positions near the boundary between two calorimeter cells. In this restricted region, selected using the energy imbalance between two neighboring cells, the calorimeter position resolution is better than 0.1 cm although the average resolution is only 1 cm. The sensitivity of the cell energy imbalance to impact position and the comparisons of the SRTD and RCAL position measurements are shown in Fig. 12. The SRTD position resolution is approximately 0.3 cm.

The SRTD position was surveyed with respect to the ZEUS coordinate system after installation. The final alignment with respect to the HERA beam coordinates was done using ep data. The spatial distribution of the energy deposit in the SRTD was considered as an "X-ray" image of the inactive material upstream. The relative position of the two SRTD halves was determined by requiring the ring image of a support structure in the end plate of the central tracking detector to be matched across the two halves. The absolute alignment was determined by requiring the scattered electron θ distribution in DIS events be independent of azimuth. The resulting alignment accuracy was 0.1 cm. The results were confirmed using the transverse momentum balance in QED Compton events.

6.2. Electron energy loss correction

The energy lost by an electron traversing inactive material upstream of the SRTD/calorimeter is related to the resulting shower-particle multiplicity, and thus to the energy deposit in the SRTD. Using both the SRTD and the calorimeter energy measurements, the electron energy loss is corrected on an event-by-event basis. This correction also reduces the degradation in energy resolution due to pre-showering in inactive material. A dedicated presampler with coarse segmentation but providing full coverage

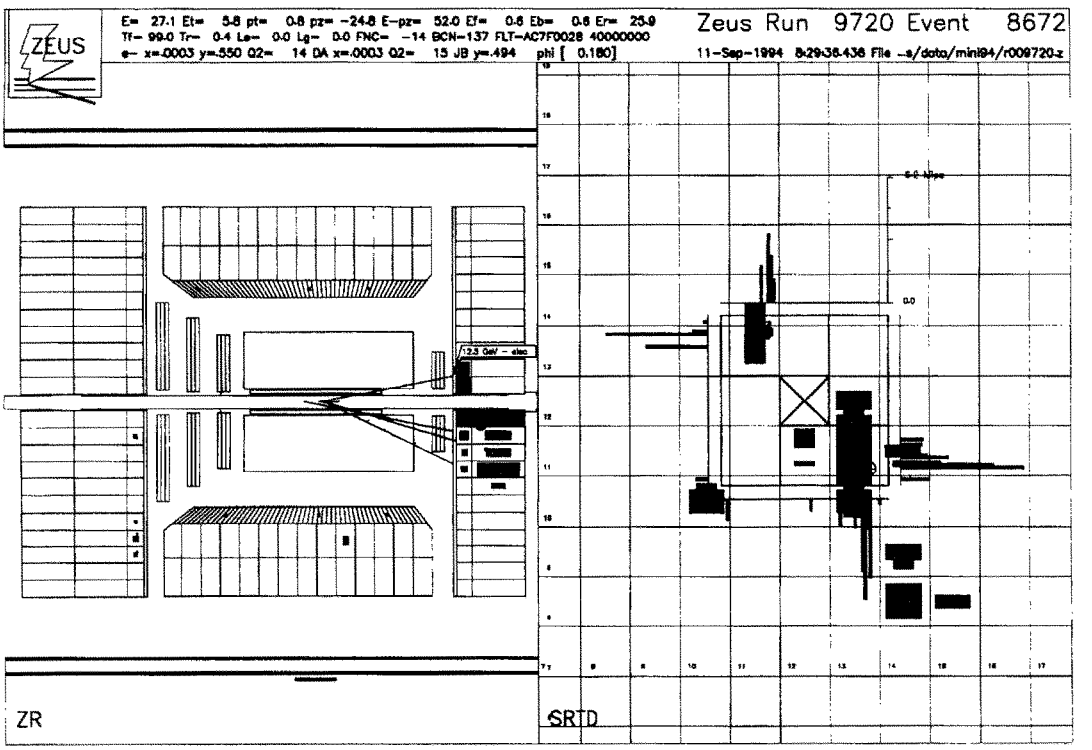

Fig. 11. Another DIS event with an electron together with hadronic activity in the SRTD. In the X–Y view (right), the SRTD strip hits are again clearly associated with the electron hit (upper left corner with respect to the beam pipe which is marked by the cross in the center). The energy deposits seen at the lower right of the beam pipe are due to particles in the hadronic system.

of the forward and rear calorimeters in ZEUS is described elsewhere [10].

In the energy correction procedure, the calorimeter and SRTD responses are related through a linear ansatz:

$$E_{\mathrm{CAL}} = a_0 + a_1 E_{\mathrm{SRTD}}, \tag{4}$$

where E_{CAL} is the electron energy measured in the calorimeter, and E_{SRTD} the total energy of the hits assigned to the electron by a clustering algorithm. In test beam studies for the ZEUS presampler [10], the parameters a_i are found to depend on both the amount of material and the initial electron energy (E_{e}). The energy dependence is parametrized by $a_i = \alpha_i + \beta_i E_{\mathrm{e}}$. The residual dependence on the amount of material is taken into account by the parametrization $\beta_1 = \mathrm{e}^{(\delta_1+\delta_2 E_{\mathrm{SRTD}})} + \mathrm{e}^{(\delta_3+\delta_4 E_{\mathrm{SRTD}})}$, chosen for optimal energy resolution. The corrected electron energy is determined using Eq. (4), by expressing E_{e} in terms of $E_{\mathrm{CAL}}, E_{\mathrm{SRTD}}$, and the correction parameters.

The energy correction parameters are determined using special classes of events in ep collisions in which the true scattered electron energy can be obtained through kinematic constraints without using the calorimeter energy information. These are:

- the kinematic peak (KP) events in DIS, in which very little momentum is transferred from the electron to the proton, and the scattered electron energy distribution peaks at the incident beam energy of 27.5 GeV;
- the elastic QED Compton events, in which the energy (in the range of 5–22 GeV) of both the final-state photon and electron can be calculated from their angles, assuming the outgoing proton carries away negligible transverse momentum; and
- the diffractive ρ^0 events in DIS, in which the momentum of the ρ^0 (reconstructed from decay pion

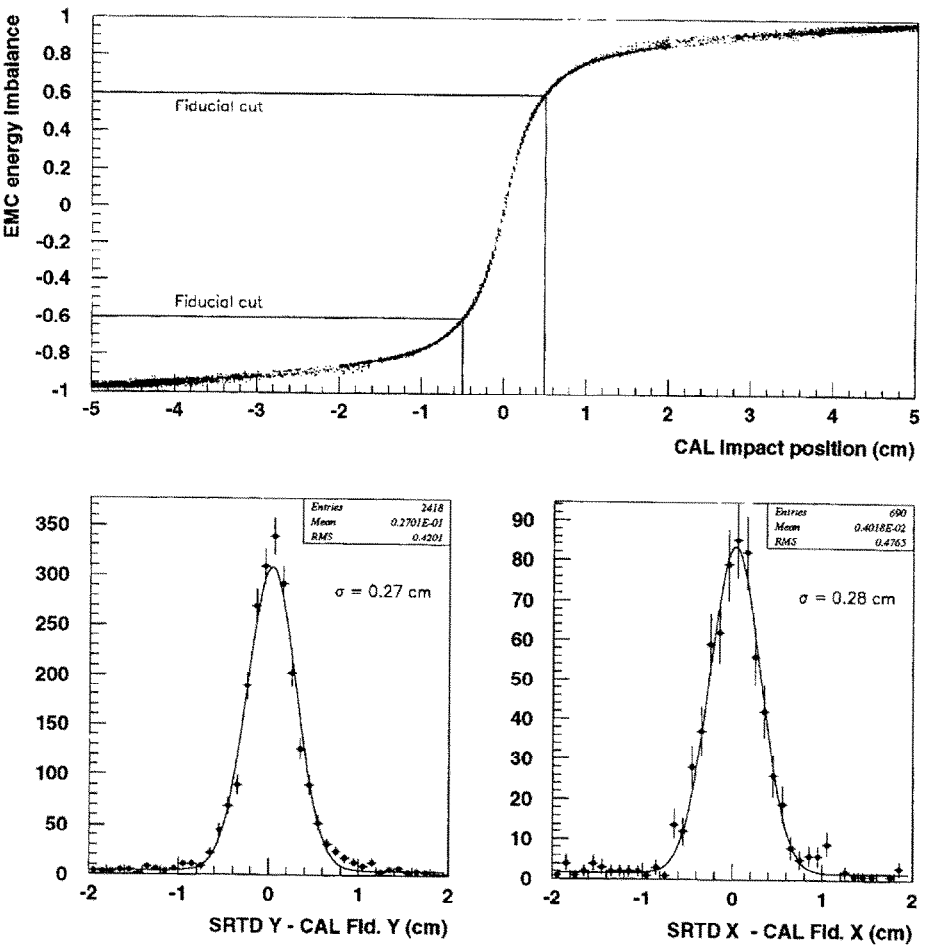

Fig. 12. Electron position measurement. RCAL cell energy imbalance versus electron impact position (top). Distributions of the SRTD-CAL Y and X positions reconstructed within the fiducial boundary region between two RCAL cells (bottom).

tracks in the central tracker) and the electron angle are used to calculate the scattered electron energy which ranges from 20 to 27.5 GeV.

The parameter values are obtained directly from the KP and elastic QED Compton events. The values for α_i and β_0 are adjusted until the difference between the corrected energy and the true energy (as given by kinematic constraints) is minimized; the values for δ_i are adjusted until the energy resolution for KP events is optimized.

The results are shown in Fig. 13. The correlation between the energy measured in the calorimeter and the energy measured in the SRTD is shown in Fig. 13(a) for KP events. The effect of the correction is shown in Fig. 13(b), where it can be seen that the KP energy distribution after correction is shifted to the beam energy with an improved resolution. The energy scale deviation of the corrected energy from the true energy, as a function of the true energy, is shown in Fig. 13(c). The corrected energy is well within 2% of the true energy. The effective energy resolution, for electrons found within the SRTD acceptance, can also be obtained from these special classes of events. It is determined from the width of a Gaussian fitted to the distribution of the difference between the corrected energy and the true energy. The result is shown as a function of the true energy in Fig. 13(d). The resolution can be described by the curve $\sigma = 26\%\sqrt{E'_e(\mathrm{GeV})}$.

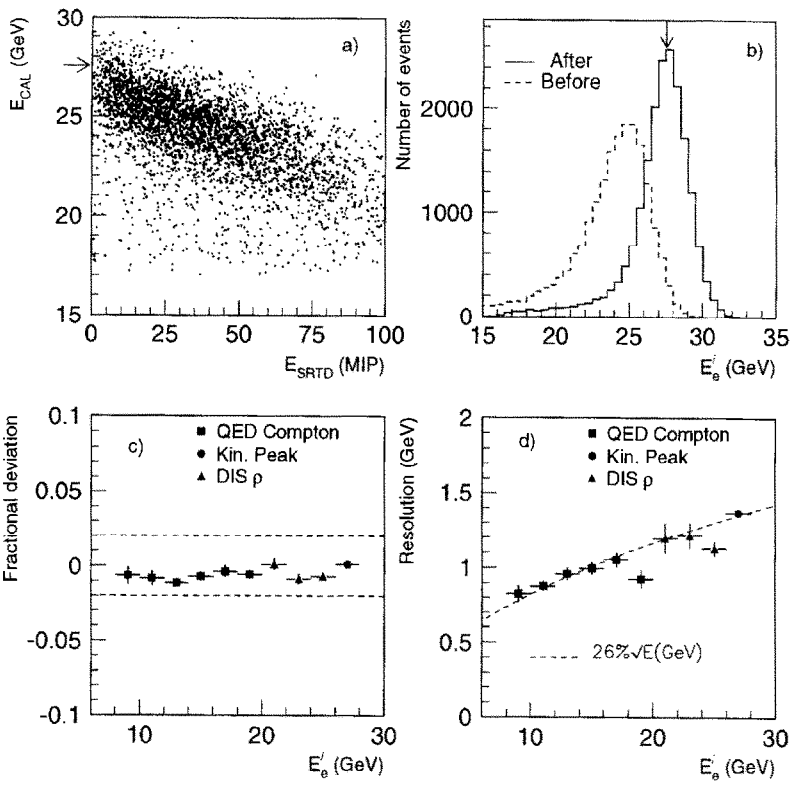

Fig. 13. Electron energy correction using the SRTD. (a) The correlation between the energy measured in the calorimeter and the energy in the SRTD for KP events. (b) The effect of energy correction for KP events. (c) The relative energy scale deviation as a function of true energy. (d) The effective energy resolution as a function of true energy. The arrows in (a) and (b) point to the beam energy of 27.5 GeV.

The DIS ρ° events are not used in the parameter tuning procedure, but are used as an independent check of the energy correction, and the results agree well with the other two data samples as shown in Figs. 13(c) and (d).

The corrected electron energy distributions, for KP events divided into several samples according to SRTD energy, are found to be identical. This is a confirmation that the dependence on the amount of material, which is related to the SRTD energy deposit, is correctly accounted for. This is important since the inactive material upstream of the calorimeter/SRTD is not uniformly distributed.

It is also important that the SRTD clustering algorithm correctly assigns hits to the electron pre-shower. In certain kinematic regions, where the scattered electrons are at low energy, the outgoing hadronic particles from the struck-quark fragmentation are likely to be found in the SRTD region. An example is shown in Fig. 11. In these events, in contrast to the clean QED Compton events used in the calibration, there are additional SRTD hits which are not related to the electron pre-shower, but are due to the hadronic particles. To investigate this effect, the energy distribution of the cluster of SRTD strips assigned to the electron is studied, and is found to be the same for both QED Compton events and standard DIS events at $E'_e = 9\,\text{GeV}$; while the energy deposit outside of the cluster increases dramatically for DIS events at $E'_e < 15\,\text{GeV}$. This is a confirmation that the clustering algorithm correctly assigns SRTD hits to the electron pre-shower for different event topologies.

6.3. *Electron timing resolution*

The offline event time distributions given by the RCAL and the SRTD are shown Fig. 14 for events with a DIS electron found in the SRTD fiducial region.

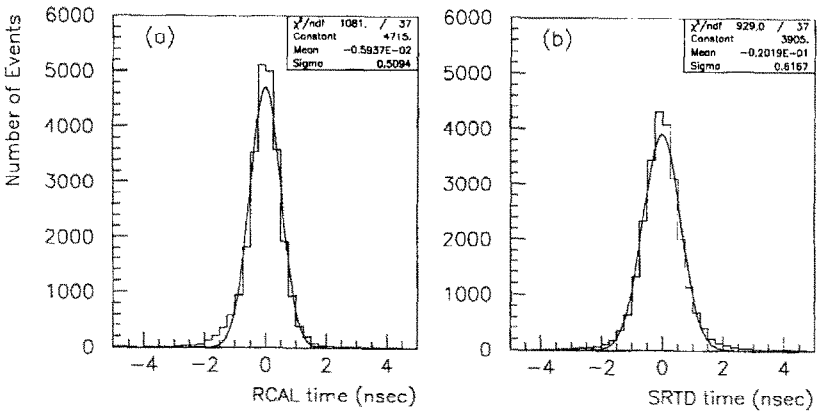

Fig. 14. Average offline timing distributions for events with a DIS electron found in the SRTD region. The RCAL (a) and the SRTD (b) show comparable timing resolutions.

The SRTD event time is averaged over all strips with energy between 0.5 and 18 MIPs, with inverse timing resolution weighting as described in Section 5.2. The electron timing resolutions given by Gaussian fits to the event time distributions are 0.51 and 0.62 ns for the RCAL and the SRTD, respectively.

6.4. *First-level trigger performance*

The SRTD online timing is used by the GFLT to veto background events. The background particles from upstream proton interactions travel along with the proton bunch and deposit energy in the RCAL and the SRTD before the proton bunch collides with the electron bunch at the interaction point. The background timing is therefore early by approximately 10 ns compared to the ep collision timing. The SRTD FLT performance is described below for the 1994 and the 1995 implementations.

6.4.1. *Performance of the SRTD FLT in 1994*

The SRTD FLT was partially instrumented in 1994 as described in Section 4.2.1. Its performance is studied using two ep data samples. One event sample satisfies all ZEUS trigger requirements, thus, containing mostly ep events; the other sample satisfies only the first-level trigger and is dominated by proton–gas backgrounds. Because of the coarse (4 ns) TDC granularity, fine tuning between the SRTD FLT time and the TDC clock of the GFLT is required. The delay is optimized to achieve the best separation between proton–gas and ep events. The correlation between the SRTD FLT timing and the RCAL timing is shown in Fig. 15. The time offsets are adjusted so that for ep events the RCAL time is approximately 0 ns and the SRTD time is at 4 TDC units. The large beam–gas background can be removed by a cut at SRTD FLT time of 6 TDC units. This cut vetoed events with timing at least 8 ns early with respect to the nominal ep collision time.

The trigger efficiencies are measured with the background events selected by RCAL timing. The thresholds are set at 12 mV (low) and 25 mV (high) to reduce noise effects while maintaining a good efficiency. The 50% efficiency point on the threshold curve is at an energy of approximately 2.8 MIPs as given by offline analysis. The combined efficiency for the 4 trigger cards is approximately 85%. The loss in ep events is estimated to be less than 0.1% from the RCAL time distributions before and after the SRTD veto. By using the SRTD FLT background veto, the FLT trigger rate associated with the RCAL is reduced by 50% and the global FLT rate by 25%.

6.4.2. *Performance of the SRTD FLT in 1995*

The SRTD FLT has been fully instrumented with new electronics since the beginning of 1995 as described in Section 4.2.2. The timing spectrum for a sample of unbiased events is shown in Fig. 16. If at least one SRTD quadrant had bad timing, consistent with a background event, and none had good timing, consistent with an ep collision, the event would be

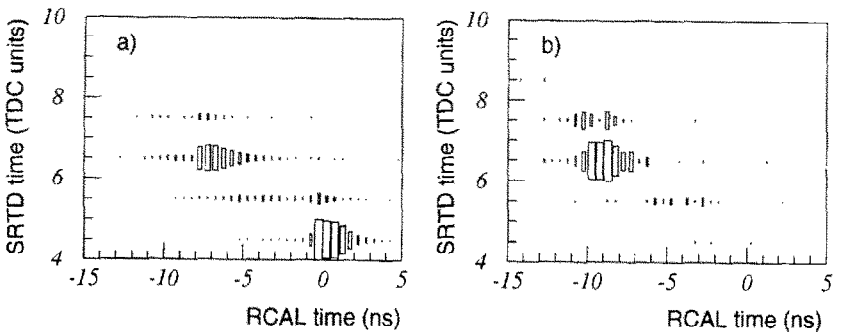

Fig. 15. Scatter plot of SRTD FLT time (TDC units) versus RCAL time (ns) for (a) all events, and (b) events dominated by proton–gas background.

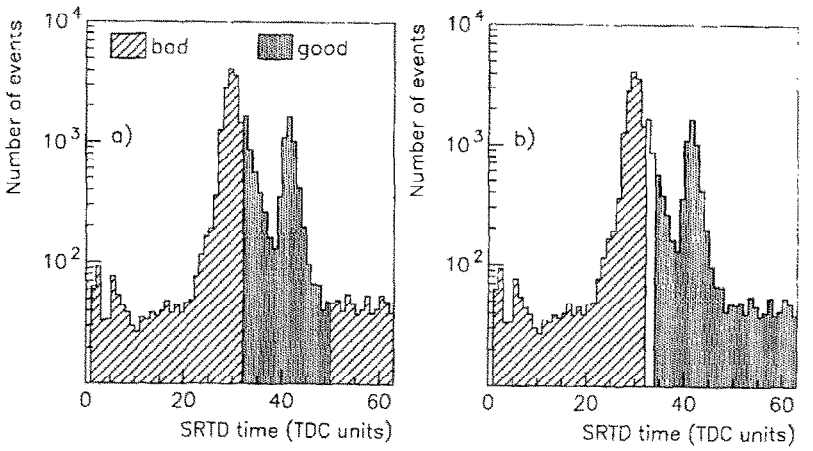

Fig. 16. Unbiased SRTD FLT timing spectrum in the 1995 run. The peak around 30 TDC units is due to proton beam–gas events, while the peak around 40 TDC units is due to ep events. The two different definitions of good and bad timing used in 1995 are illustrated.

vetoed. Two versions of the veto logic were used in the running period. Initially, good timing was defined to be $32 \leq t \leq 49$ and bad timing was defined to be $t < 32$ or $49 < t < 63$, where t is the SRTD FLT time measured in TDC units of (1.00 ± 0.05) ns. This is illustrated in Fig. 16(a). Later in the year, the good-timing upper limit was relaxed while the lower limit was tightened: $34 \leq t \leq 63$ (see Fig. 16(b)). This change resulted in more late-timing physics events being accepted while maintaining a low background rate. Using the SRTD FLT timing information, the GFLT rate was reduced by a factor of 3 to 4 for both versions of the veto logic. In particular, the SRTD FLT veto nearly compensated for the sharp increase in the RCAL electron trigger rate which was due to the reduction of the vertical gap in the RCAL beam pipe region. The loss in ep events was estimated from an unbiased sample to be less than 0.5%.

Because the timing resolution degrades for small signal pulses and the presence of electronics noise at the 0.1 MIP level, the discriminator high thresholds are set to approximately 0.5 MIP. The trigger efficiency is studied using data. It is measured by the fraction of the time the TDC is stopped with a coincidence signal when one scintillator layer registers at least 1.0 MIP while the overlapping layer registers a maximum energy deposit in the strips ranging from 0 to 1.5 MIPs. The trigger efficiency is shown in Fig. 17 as a function of the effective threshold setting. The timing resolution is determined from a fit to the TDC

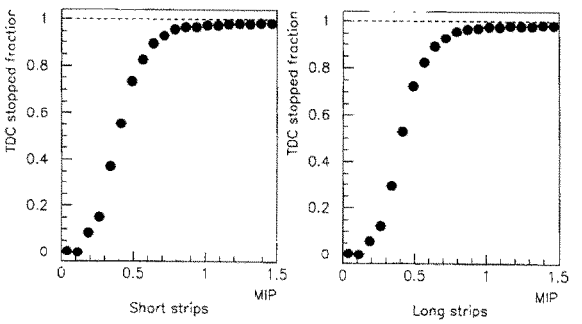

Fig. 17. The fraction of nonoverflow SRTD FLT TDC outputs as a function of the maximum strip energy in one plane of strips when the other plane registers at least 1.0 MIP.

distribution around the ep time for events passing all the ZEUS trigger requirements. The overall timing resolution is approximately 1.5 ns, including a residual run-to-run variation on the HERA timing and the differences (approximately 0.5 ns) between the four quadrants; while the timing resolution for a typical quadrant in a given run is approximately 1.4 ns. The results are shown in Fig. 18.

6.5. The impact on F_2 measurement

As mentioned in Section 1, it is of great interest to extend the measurement of the proton structure function $F_2(x, Q^2)$ to the region $x < 10^{-4}$. Because of HERA kinematics, in the small x region of interest, the electron is scattered at small angles. Furthermore, the struck quark, carrying a small fraction of the incoming proton's momentum, is also scattered into the backward direction. Prior to the availability of the SRTD, the ZEUS F_2 measurements relied on the "double-angle" method to reconstruct the kinematic quantities, mainly due to the lack of reliable electron measurements [2]. This method uses the measured angle of the hadronic system and the angle of the scattered electron to reconstruct the kinematic variables, and is therefore insensitive to the electron energy measurement. However, in the small x region, the x and Q^2 reconstructed with this method suffered from large systematic shifts and coarse resolutions because the hadronic system was not well measured due to particles escaping through the rear-beam hole, and because near the RCAL boundary around the beam pipe the electron angle was not reliably determined due to shower leakage and coarse calorimeter segmentation. As a result, the region where $F_2(x, Q^2)$ could be measured reliably was restricted to $x > 4.2 \times 10^{-4}$, even though events with lower x were detected.

With the SRTD, as shown in the previous sections, the electron energy and angle measurements in the angular region around the RCAL beam pipe, corre-

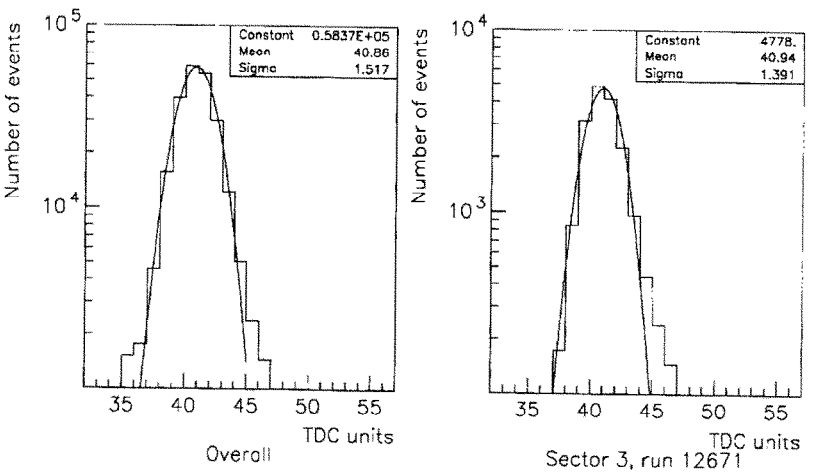

Fig. 18. SRTD FLT timing resolution in 1995: overall timing including quadrant-to-quadrant and run-to-run variations (left), and timing for a typical quadrant in a single run (right).

sponding to small x, are now well understood. During the 1994 running period, the ep collision vertex was shifted further away from the RCAL, resulting in an increase in the geometric acceptance for low x events. With x and Q^2 reconstructed from electrons in the SRTD region, the structure function was measured at $x = 3.5 \times 10^{-5}$, with a systematic uncertainty of $\pm 10\%$ [11].

7. Summary and outlook

The design, construction, installation, and performance of the small angle rear tracking detector of the ZEUS experiment at the HERA electron–proton collider have been described. It consists of finely segmented scintillator strips read out by photomultipliers via plastic fiber light guides. The impact position of the scattered electron in deep inelastic events is measured with a 0.3 cm resolution. The SRTD is aligned with respect to the HERA beam axis with a 0.1 cm accuracy. The SRTD is also used to correct the electron energy loss due to pre-showering in an inactive material in front of the calorimeter. The electron energy is corrected to well within 2% of the true energy for an electron energy in the range 8–27.5 GeV, while at the same time improving the measured energy resolution. With the improved measurement of the scattered electron in the small-angle region, the proton structure function $F_2(x, Q^2)$ has been determined at $x \sim 10^{-5}$ from ZEUS data collected during the 1994 running period.

The SRTD online timing, with a resolution of better than 1.5 ns, is used at the first-level trigger to veto backgrounds from upstream proton–gas interactions. As a result, the ZEUS global FLT rate was reduced by 25% with a partially instrumented SRTD FLT in 1994, and by a factor of 3–4 with a fully instrumented SRTD FLT in 1995. Starting in the 1996 running period, the SRTD FLT has also been used in coincidence with the RCAL FLT to accept events with the signature of a low-energy DIS electron scattered at small angles. The performance of the SRTD FLT hardware has been stable. All branches of the physics trigger logic in the GFLT now include the SRTD FLT veto in order to maintain reasonable rates with the increasing instantaneous luminosity provided by HERA.

Acknowledgements

We would like to thank the DESY Directorate for its strong support. We would also like to thank the following people who helped in the construction, installation, and data analysis: N. Bishop, B. Dabrowski, W. Drayer, C. Farrow, N. Feind, C. Foudas, M. Gospic, H. Groenstege, C. Hartmann, Y. Iga, F. Jedrzejowski, C. Keyser, J. Labs, K. Löffler, A. Maniatis, U. Mick, C. Muhl, W. Schulz, W. Sippach, M. Sowinski, H. Stehfest, J. Thiesing, K. Tokushuku, and N. Wilfert.

References

[1] ZEUS collaboration, The ZEUS Detector, Status Report 1993, DESY, 1993.
[2] ZEUS collaboration, M. Derrick et al., Phys. Lett. B 316 (1993) 412; Z. f. Phys. C 65 (1995) 379; H1 Collaboration, I. Abt et al., Nucl. Phys. B 407 (1993) 515; Nucl. Phys. B 439 (1995) 471.
[3] L. Hubbeling, CERN EP-78-5, ECP-92-10.
[4] M. Gospic, H. Groenstege, NIKHEF Note ETR 94-11.
[5] B. Lu et al., Nucl. Instr. and Meth. A 313 (1992) 135.
[6] T. Ishii et al., Nucl. Instr. and Meth. A 320 (1992) 449.
[7] A. Caldwell et al., Nucl. Instr. and Meth. A 321 (1992) 356.
[8] J.W. Dawson et al., IEEE NSS Conf. Record, vol. 1, 1995, p. 427.
[9] J.E. Moyal, Philos. Mag. 46 (1955) 263.
[10] A. Bamberger et al., Nucl. Instr. and Meth. A 382 (1996) 419.
[11] ZEUS collaboration, M. Derrick et al., Z. f. Phys. C 69 (1996) 607.